ORIGINAL PAPER-EXPLORATION GEOPHYSICS

Electrical properties of sedimentary microfacies and depositional environment deduced from core analysis of the syn-rift sediments, Northwestern shore of Gulf of Suez, Egypt

Emad A. Abd El Aziz[1] · Mohamed M. Gomaa[1]

Abstract

The present work is based mainly on core rock samples investigation of CSS-38 well, northwest of Gulf of Suez, Egypt. The cores cover the whole the South Gharib Formation (upper Miocene). The stratigraphic succession of the Gulf of Suez includes three mega units, recorded from old to young as pre-rift, syn-rift, and post-rift sediments. The syn-rift sediments from old to young are Nukhul, Rudies, Kareem, Belayim Equivalent, South Gharib, and Zeit. The core samples reveal that South Gharib Formation is not a good reservoir. It consists of sulphate-rich beds with few carbonates intercalation, laminated dolomitic limestone and marly limestone. Patchy oil staining is detected in the thin streaks and basal laminated dolomitic limestone. The microfacies are found to be evaporites, carbonates, calcareous marl, and calcareous claystone. Evaporites microfacies are considered the most frequent microfacies. Gypsum and anhydrite are generally represented by nearly equal distribution with parallel variation in content. The core samples differentiated South Gharib Formation into seven zones of depositional environment; they are arranged from base to top as shallow sub-tidal, shallow lagoonal, intertidal, shallow lagoonal, intertidal, shallow lagoonal, and supra-tidal Sabkha cycles. Some samples from South Gharib Formation were measured electrically. We will try to highlight interrelations between electrical (conductivity, permittivity, and impedance) and petrophysical properties with petrography and mineral composition. Electrical properties were measured with a frequency range from 10 Hz to 100 kHz. The dielectric constant decreases with increasing frequency and increases with increasing conductor content (up to percolation threshold). The conductivity increases with the increase in conductor content and with increasing frequency. Many parameters can combine to affect electrical properties. The present research is a trial to relate the surface to subsurface measurements.

Keywords Petrography · Sedimentary microfacies · Conductivity · Dielectric constant · Frequency domain · Sandstone

Abbreviations

ω	Angular frequency	σ_g	Grain density
σ_b	Bulk density	ε''	Imaginary relative permittivity
Z	Complex impedance	C_p	Parallel capacitance
ε^*	Complex relative permittivity	G_p	Parallel conductance
A	Cross-sectional area	P_C	Percolation threshold
n	Curve slope	k	Permeability
W_d	Dry sample weight	ε_0	Permittivity of free space
Q	Flow rate	V_p	Pore space volume percentage
μ	Fluid viscosity	φ	Porosity
		ΔP	Pressure gradient
		X	Reactance
		σ'	Real conductivity
		ε'	Real relative permittivity
		R	Resistance
		L	Sample length
		V_b	Total sample volume
		V_g	Volume of grain

✉ Mohamed M. Gomaa
mmmsgomaa@yahoo.com

1 Geophysical Exploration Group, Geophysical Sciences Department, National Research Centre, National Institute of Oceanography & Fisheries (NIOF), El-Behoos St, Dokki, Cairo, Egypt

Introduction

Engineering geologists need to know some information about the nature of the reservoir rocks in order to develop and expand production in oil wells, particularly from the facies and diagenetic points of view. This sort of inquiry also contributes to a preliminary knowledge of the reservoir quality of the various strata of host rock. Many research have been conducted on the infracambrian source rocks. (Saber 2012; Ashraf et al. 2019, 2021; Sallam and Ruban 2020; Radwan et al. 2020; Shehata et al. 2021; Vo Thanh and Sugai, 2021; Anees et al. 2022a, b; Vo Thanh and Lee 2022). The Gulf of Suez was developed during the early Paleozoic period as a subsidence basin inside the stable shelf. Then, in the lower to middle Tertiary, it is strongly reactivated during the rifting period of the vast African rift system (Bakr and Wilkes, 2002). Two orthogonal normal fault systems run parallel to each other in the Gulf of Suez, one parallel to the Gulf of Suez and the other parallel to the Gulf of Aqaba. Five big tectonic events impacted the Gulf of Suez (Leila and Moscariello, 2018). Due to a rapidly sinking depression, a large amount of silt has accumulated in the Gulf of Suez (Said, 1990; EGPC, 1996). Major hydrocarbon accumulations, reservoir facies, and seal rock may all be found in the syn-rift sediments (Khalil and Mesheref, 1988). Evaporites from the Miocene epoch are regarded as the height of evaporites formation. The study aims to identify the syn-rift sedimentary facies types, textural, mineralogical composition, and depositional environment encountered in the studied section of the northwestern shore of the Gulf of Suez.

The majority of the heavy oil accumulations in the Gulf of Suez's Issaran field are trapped in Miocene cracked carbonate and siliciclastic reservoirs. Because of the presence of well-exposed and reasonably well-dated syn-rift marine layers, as well as the huge quantity of exploration data available, the Gulf of Suez has been the site of several sedimentological and structural investigations of rift evolution. Terrigenous clastics from the unroofing of the elevated rift flanks or shoulders dominate the early and middle Miocene syn-rift sedimentary periods. These successions are among the Suez province's most prolific petroleum reserves. For accurate development and prediction in continuing exploration, a full understanding of their depositional history and governing elements is essential. Ashraf et al. (2019) demonstrate that the Sawan Gas field's thin shale sequence is interbedded and scattered, resulting in severe variability. As a result, traditional seismic amplitude interpretation fails to identify the spread of sand-shale facies. According to the electrofacies studies, the reservoir C-sand interval follows funnel-shaped, bell-shaped, and cylindrical-shaped tendencies. Multiple seismic characteristics were used to analyse the C-sand interval. The calibration of electrofacies analysis with 3D seismic attributes shows a good agreement between them and predicts the geographical distribution of sweet spots in a heterogeneous reservoir using 3D seismic attributes analysis.

It is usual to evaluate hydrocarbon production from exceedingly diverse or poor-quality reservoir rocks (Ashraf et al. 2019, 2021; Anees et al. 2022a, b; Vo Thanh and Sugai, 2021; Vo Thanh and Lee 2022). Understanding the depositional environmental and geological influences on these low-quality reservoir rocks is critical for economic evaluations (Ashraf et al. 2019). In recent years, lithological information from well log replies, including pattern identification and pattern classification, has been collected (Anees et al. 2022a, b; Vo Thanh and Lee 2022). The Gamma-Ray (GR), Spontaneous Potential (SP), and resistivity log responses were included to examine depositional settings and the association between depositional facies for hydrocarbon exploration in order to maximise the advantages of conventional well logs. Based on well log responses, electrofacies is a useful method for dividing the formation into facies. As the nature of the log is strongly connected to the grain size of rock sequences, Ashraf et al. (2019) investigated the morphologies of well log curves as a method to derive depositional facies. Several case studies have been successfully used to investigate the depositional sedimentary environments of reservoirs in preparation for field exploration and development. A more accurate categorization of the sand-shale facies' depositional context based on well log facies analysis and seismic attribute association is critical for prospect identification, appraisal, and field development. The terminology used in the classification of the different microfacies types and depositional textures of the carbonate encountered in the studied section is based on Folk (1959 and 1962); Dunham (1962); Embry and Klovan (1971); and James (1984). The terminology used to describe the crystallization and textures of the sulphate minerals and nodules is based on Shearman and Fuller (1969), Cody and Cody (1988), and Warren (2006). The description of the different porosity types follows Choquette and Pray (1970).

Electrical energy conduction (and dissipation) and electrical energy storage are characterized by the electrical characteristics of materials. Electrical conductivity, as defined by geometry, characterizes a material's capacity to transmit charge via conduction. Electrical dissipation is caused by charge transfer or conduction. Dissipation or energy loss is caused by the conversion of electrical energy to thermal energy during collisions as the charges travel. The outcome of charge storing energy is electrical storage (dielectric polarization or dielectric permittivity). Charge mobility is dissipative as polarization occurs and causes charges to migrate.

To fulfil this purpose, conventional petrographic microscope examination of core rock samples of CSS-38 well was chosen for that (Fig. 1). Also, some electrical measurements were measured with a frequency range from 10 Hz to 100 kHz on some hand specimen samples from the south Gharib Formation.

First, the method is presented. Then, we study the microfacies and other related parameters of the well. Finally, the electrical properties was measured and discussed in detail.

Geology and tectonics of the Gulf of Suez rift

The Suez Gulf is a rifted basin in which tectonic activity has had a significant impact on the sedimentological and stratigraphic expression of rift-related strata. The fault extension-induced evolution has a main influence on sedimentation, affecting both fluid flow and the formation of deposition sites. The rifting of the Gulf of Suez began in the late early Miocene. Early syn-rift igneous rocks from the Gulf of Suez have been radiometrically dated to 24–21 Ma (early Miocene), whereas Patton et al. have examined the oldest Miocene and Oligocene rift-related faulting (1994). Apatite fission track ages of granitic basement suggest significant uplift of the Red Sea Hills to the west of the Gulf of Suez, which is related with early rifting about 21–23 Ma (early Miocene). High relief and coarse-grained alluvial deposits developed from extensional movements along the northwestern Red Sea coast and early Miocene tilting of Gebel el Zeit fault blocks. Sedimentation was concentrated in high accommodation regions near active faults. Changes in depositional conditions were greatly impacted by varying fault activity along bounding faults. In the late-lower to early-middle Miocene, deep-water successions of the Rudeis and Kareem formations were deposited as a result of continued extension accompanied with significant regional subsidence and accompanying transgression. In the late Miocene–Pliocene, further rifting and sinking occurred in the southern Gulf of Suez, leading in the deposition of the Belayim, South Gharib, and Zeit formations. Faulting within the Pleistocene successions, where outcrops of Pleistocene reefs and ooid sand are observed up to 150 m above current sea level, demonstrates late Pleistocene–Holocene deformation in Gebel el Zeit. Because relatively early Pleistocene reefal deposits are located on the east side of Gebel el Zeit 10–18 m (32.8–59.04 ft) above sea level but are not elevated at Zeit Bay to the southwest, the late Pleistocene–Holocene uplift appears to be related with tilting (Evans 1990). Active faulting is shown in modern earthquakes in the area. The present Gulf of Suez area has remarkable topographic relief, with denuded basement rising to over 2000 m (6560 ft) on the sides. More

Fig. 1 Location map showing the CSS-38 well, Issaran Field, Gulf of Suez, Egypt

than 5000 m (16,400 ft) of Neogene Syn-rift sediments may be found in the depocenters along the axial trough.

General depositional setting of Syn-rift sediment of the Gulf of Suez

The tectonic setting of the Gulf of Suez is considered the main factor that controls the distribution of the Miocene sediments. The rapid lateral changes in thickness and facies of the syn-rift Miocene sediments could be the result of differential movements of the Pre-Cambrian blocks (Sellwood and Netherwood, 1984).

The syn-rift Miocene sediments include two groups, named Gharandal and Ras Malaab. The Lower-Middle Miocene Gharandal Group (clastic phases) is differentiated from base to top into Nukhul, Rudeis, and Kareem Formations. The Ras Malaab Group (Middle-Upper Miocene) includes upward Belayium, South Gharib, and Zeit Formations (Evans 1988a, b; El-Ghali et al. 2013). The Miocene sediments exhibit rapid facies change, where rapid subsidence is accompanied by major marine transgression and the deposition of thick mixed carbonates, clastics, and evaporates in the rift and deeper parts of the basin (Zaid, 2013). The lower Miocene clastics were unconformably deposited on the Pre Miocene Formations on the tilted surfaces of the fault blocks between the structural lows of the Gulf of Suez and in the northern part of the red sea.

The rapid rate of sedimentation with their considerable thickness and organic shale content favoured them as very suitable source rocks. High energy carbonate build-ups were developed along the high edges of the uplifted fault blocks. The Middle Miocene is represented by the imminent evaporatic series development especially in the margins of the Gulf basin. Along the margins of the grabens, thick calcareous and anhydritic sequences are formed giving a thick salt basinward. The thickest salt is deposited near the junction of the red sea and Gulf of Suez (EGPC, 1996). The Middle Miocene is represented by a drastic change in the cycle from the heavy fluvial to the extremely arid evaporitic sequence.

The influx of clastics had slowed down considerably during deposition of the Belayim Formation and was almost completely shut off during precipitation of South Gharib evaporates. Zeit Formation sequence represents a return to the state of intermittent sedimentation of clastics during evaporates cycle (Moustafa, 1996).

Litho-stratigraphy

The Gulf of Suez rift includes three mega units arranged from bottom to top into pre-rift, syn-rift and post-rift sequences. The sequence of syn-rift sediments includes a

red bed clastic section of Abu-Zenima Formation that is related to the Oligocene-Early Miocene age. Abu-Zenima Formation is overlaid by Miocene sediments that include two facies: first one; clastics predominance section including Nukhul, Rudeis, and Kareem Formations and the second is evaporites predominance section that constituent mainly from anhydrite and salt including Belayim, South Gharib, and Zeit Formations (Abul-Nasr 1990).

The Miocene section represents marginal facies which includes five main formations arranged from top to bottom as Zeit sand, South Gharib, two dolomite units (Belayim equivalent), Gharandal, and Nukhul carbonates. The investigation from the core samples reveals that South Gharib Formation consists predominantly of sulphates grading upwards into sulphate-rich beds in the upper part, with few carbonates intercalation. Laminated dolomitic limestone, with evaporites, is grading downwards into laminated dolomitic limestone and marly limestone in the lower part. Patchy oil staining is detected in the thin streaks and basal laminated dolomitic limestone. South Gharib Formation (target of the study) conformably underlies the Zeit Formation and unconformably overlies the upper dolomite rock unit (Fig. 2).

Methodology

The core samples of the south Gharib Formation were investigated under plane-polarized light by the conventional petrographic microscope to identify the types of sedimentary facies, mineralogical compositions, textural and depositional environment. The preparation of the thin sections was performed at Corex laboratories, Egypt. Alizarin Red S was used to differentiate calcite (stained purple) from dolomite (unstained). Moreover, Methylene blue dye was used to identify the intensity and types of porosity in the studied thin sections, whereas sodium cobalt nitrate solution was used for the identification of feldspars (Corex, 2009). Forty-eight samples were selected for microscopic investigation. They represent the different facies types, textures composition, depositional environment encountered at the south Gharib section of the northwestern shore of the Gulf of Suez, Egypt. Two core numbers 1 and 2 with total thickness 106 feet covered these intervals (Core No. 1: 960.00′–1021.06′ = 61.5 ft., Core No. 2: 1021.06′–1066.00′ = 44.5 ft.).

Nineteen samples were selected from CSS-38 well, and Cores 1 and 2 were subjected to X-Ray Diffraction (XRD) analyses. The samples were measured using an X-Ray diffract metre. PRUKUR D 8 ADVANCE with Cu K target with secondary monochromator (Kv. = 45, MA = 40, 2θ range was 4°–70°) (Corex, 2009).
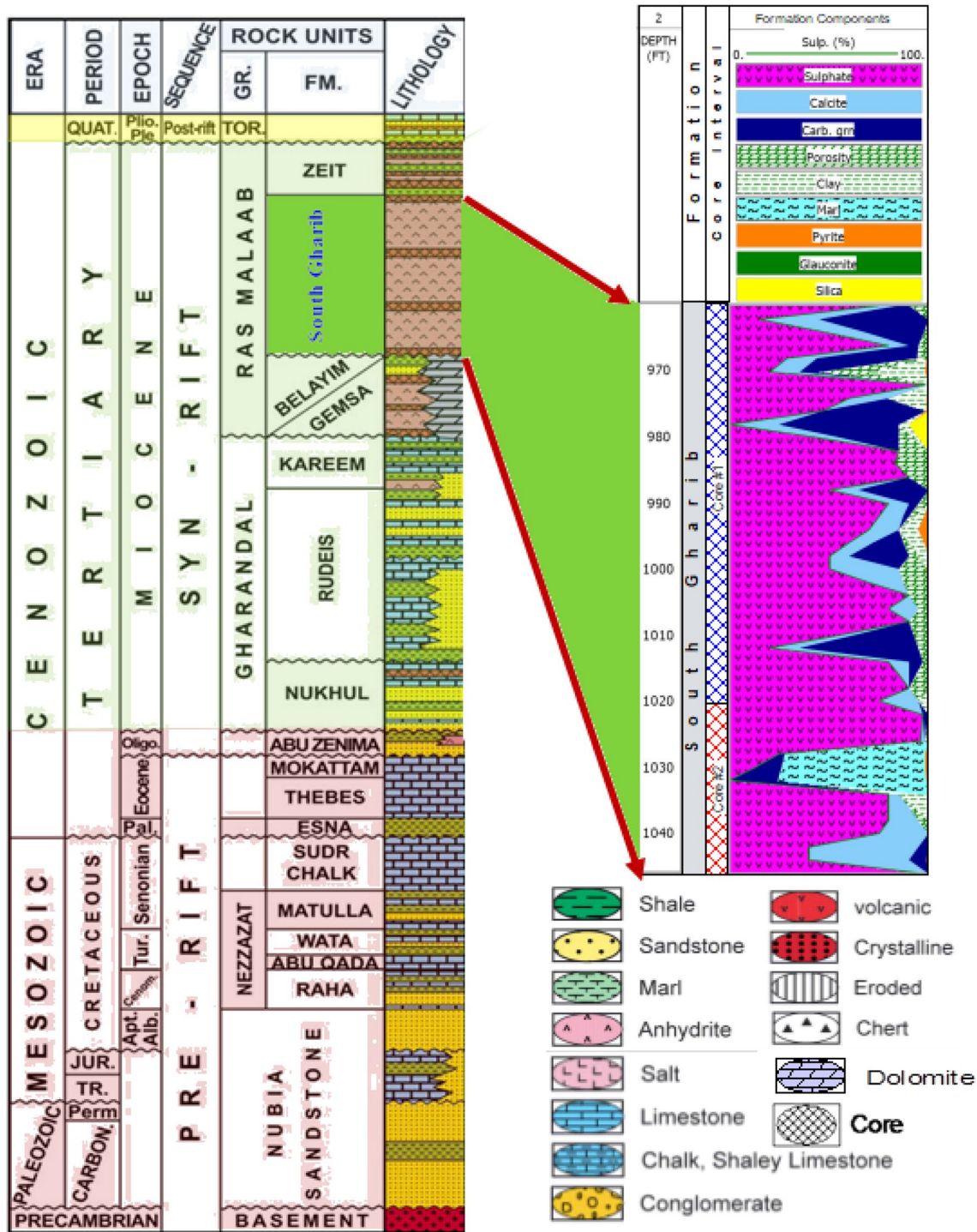
Fig. 2 Simplified stratigraphic section of the Gulf of Suez (South Gharib Formation), with detailed syn-rift Miocene lithology components (Modified after Saoudi et al. 2014)

Electrical and petrophysics instruments

Both a matrix-cup helium porosimeter (gas-expansion method) and a DEB-200 instrument (Archimedes' principle) were used to determine porosity for the samples. The details of the petrophysical calculations will be discussed later (Sect. 5.9).

For electrical measurements, the thickness and area of samples were prepared to be at least 1:5 to avoid stray capacitance. The specimen faces were adjusted to have

parallel faces. Hioki 3522-50 LCR instrument was used (10 Hz–100 kHz) using non-polarizing electrodes (Cu/CuSO$_4$) (Gomaa 2008, 2013; Gomaa and Alikaj 2010). Measurements were made at the humidity of (45%) and room temperature (24 °C) in an isolated chamber (Gomaa 2009 and Shaltout et al. 2012).

Electrical properties were measured in parallel arrangement [parallel capacitance (C_p) and parallel conductance (G_p)]. The complex relative permittivity $\varepsilon *$ is

$$\varepsilon^* = \varepsilon' - i\varepsilon'' \tag{1}$$

Measured relative permittivity (ε') is

$$\varepsilon' = \frac{C_p d}{\varepsilon_0 A} \tag{2}$$

Imaginary relative permittivity (ε'') is

$$\varepsilon'' = \frac{G_p d}{\omega \varepsilon_0 A} \tag{3}$$

where ε_0 is the permittivity of free space (8.85×10^{-12} F/m), and ω is the angular frequency. Real conductivity is

$$\sigma' = G_p \frac{d}{A} = \varepsilon'' \omega \varepsilon_0 \tag{4}$$

The complex impedance (Z)

$$Z = R - iX \tag{5}$$

where X is the reactance and R is the resistance.

Results of South Gharib formation

Sedimentary microfacies of the South Gharib Formation

The syn-rift sedimentary section of the South Gharib Formation has been studied with the aid of two continuous core numbers 1 and 2 with a total thickness of 106 feet that cover these intervals (Core No. 1: 960.00′–1021.06′ = 61.5 ft., Core No. 2: 1021.06′–1066.00′ = 44.5 ft.). Based on a detailed examination of the obtained thin sections, the sedimentary facies of the studied formation can be differentiated into four microfacies types as will be discussed briefly as follows

Evaporitic microfacies

These microfacies represent the most frequent microfacies in both cores 1 and 2 (Figs. 3, 4). It is composed mainly of anhydrite, gypsum, and celestite minerals. All the evaporite microfacies show remnants of the displaced and replaced carbonates enclosed between the nodules. The inter-crystalline porosity type is dominant in sulphate microfacies which are mainly confined to the carbonate remnants and much less dominant between the anhydrite laths as described briefly in the following.

a. Anhydrite: Anhydrite microfacies are represented by anhydrite nodules composed of microcrystalline anhydrite which is developed into lath-shaped crystals (0.1–3 mm long). The lath crystals are arranged either in a decussate fabric or as rosette-like aggregates which developed either perpendicular or parallel to lamination. Anhydrite laths are arranged sub-parallel to the periphery of the nodule. Palmate anhydrite forms are also recorded (Fig. 4b). Anhydrite laths replace and displace the carbonate stringers (Figs. 3 and 4).

b. Gypsum: The examined thin sections reflect three forms of gypsum. The first; is the partly or completely replaces the anhydrite decussate and radiating laths, attaining their original form. The second; is the Rosey gypsum replacing both the anhydrite and gypsum laths and composed of very fine fibrous crystals. The third; is the porphyritic gypsum (millimeters to several centimeters in scale) replacing both the original anhydrite and the replacing gypsum, as well as the carbonate stringers separating the evaporite nodules. Corroded remnants of all these replaced components are encountered enclosed in the porphyritic gypsum. Porphyritic gypsum replaces the greater part of fossil fragments and the groundmass (Figs. 3 and 4).

c. Celestite: The third type of evaporite mineral encountered in the studied formation is the granular celestite anhedral crystals (maximum 0.1 mm diameter) that displaces and replaces the calcareous claystone and the carbonate crystals. It is recorded in the upper part of the studied formation and confirmed also by X-ray diffraction (XRD) analysis (Fig. 3b).

Carbonate microfacies

Thin carbonate beds are intercalated by sulphate-rich beds. This is recorded in 7 samples out of the 29 samples of the upper part (963.02, 965.06, 968.04, 970.00, 978.10, 991.08, 999.05, and 1011.08 feet) and in 2 samples only out of the 19 samples of the lower part (1042.07 and 1044.02 feet). The carbonate microfacies are represented either by the thin stringers separating the evaporitic nodules or by scattered remaining small corroded patches replaced by the evaporites. It is composed mainly of dolosparite, dolomitic microsparite, dolomitic micrite, or finely crystalline calcite mixed with clayey material. The two carbonate beds of the lower part are of the microsparitic type, scattered dolomite crystals, beside sulphatized intraclasts and recrystallized pellets (0.05–0.2 mm in diameter), foraminifera, bryozoans, and bioclasts (up to 0.7 mm) all these are embedded in dolomicrite, microsparite to partly dolomitic microsparite
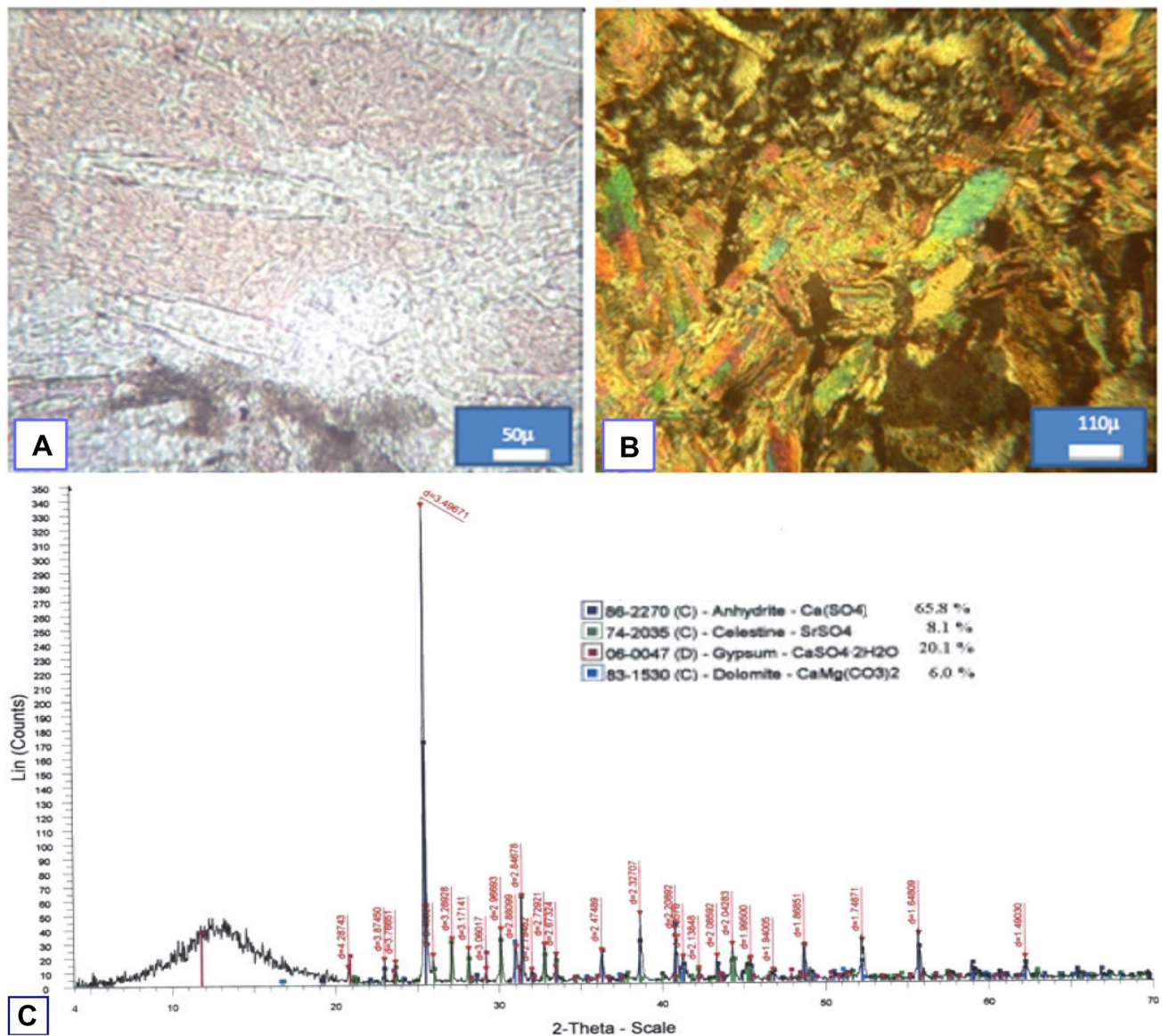
Fig. 3 Evaporitic microfacies of the South Gharib Formation: **A** Two evaporite generations are exhibited; a colourless one and a later replacing pink one. Darker remnants of the original carbonate appear at the central bottom part of the photo (Plane Polarized Light; X200), Depth: 983 ft. **B** Decussate anhydrite laths and those laths sub-parallel to a nodule at the left side of the photo (with high interference colours). The upper central part shows a celestite mosaic (with grey interference colours). Porphyrotopic gypsum fills the lower right corner (between crossed Nicols, X110), Depth: 983.00 ft. **C** The examined minerals through X-ray diffraction (XRD) Patterns, Depth: 983 ft

groundmass forming a wackestone, packstone, framestone depositional texture. Few pyrite and glauconite grains are also found scattered in the groundmass. Their porosity reaches 20% and is of the inter-crystalline, intra-particle, micro fracturing, or moldic type (Fig. 5).

The carbonates facies are mainly bioclastic and intraclastic, and few only are pellets or foraminiferal. Two thin sections including microbially laminated microfacies were recorded among these carbonates. The bioclasts are represented by considerable variation in size from a fraction of millimeters up to 4 mm in length. The fine bioclasts are undifferentiated and obvious that a considerable amount of the bioclasts were subjected to dissolution. Coarser ones are generally replaced by anhydrite and gypsum. Almost all of the fossil fragments were dissolved and now replaced by anhydrite and/or gypsum which occlude the porosity. The fossils and fossil fragments encountered are ranging in size between 0.3 to 9 mm. They are composed of benthic foraminifera, gastropods, bivalves, bryozoans, and corals. They partly show dolomitization, but most of them are
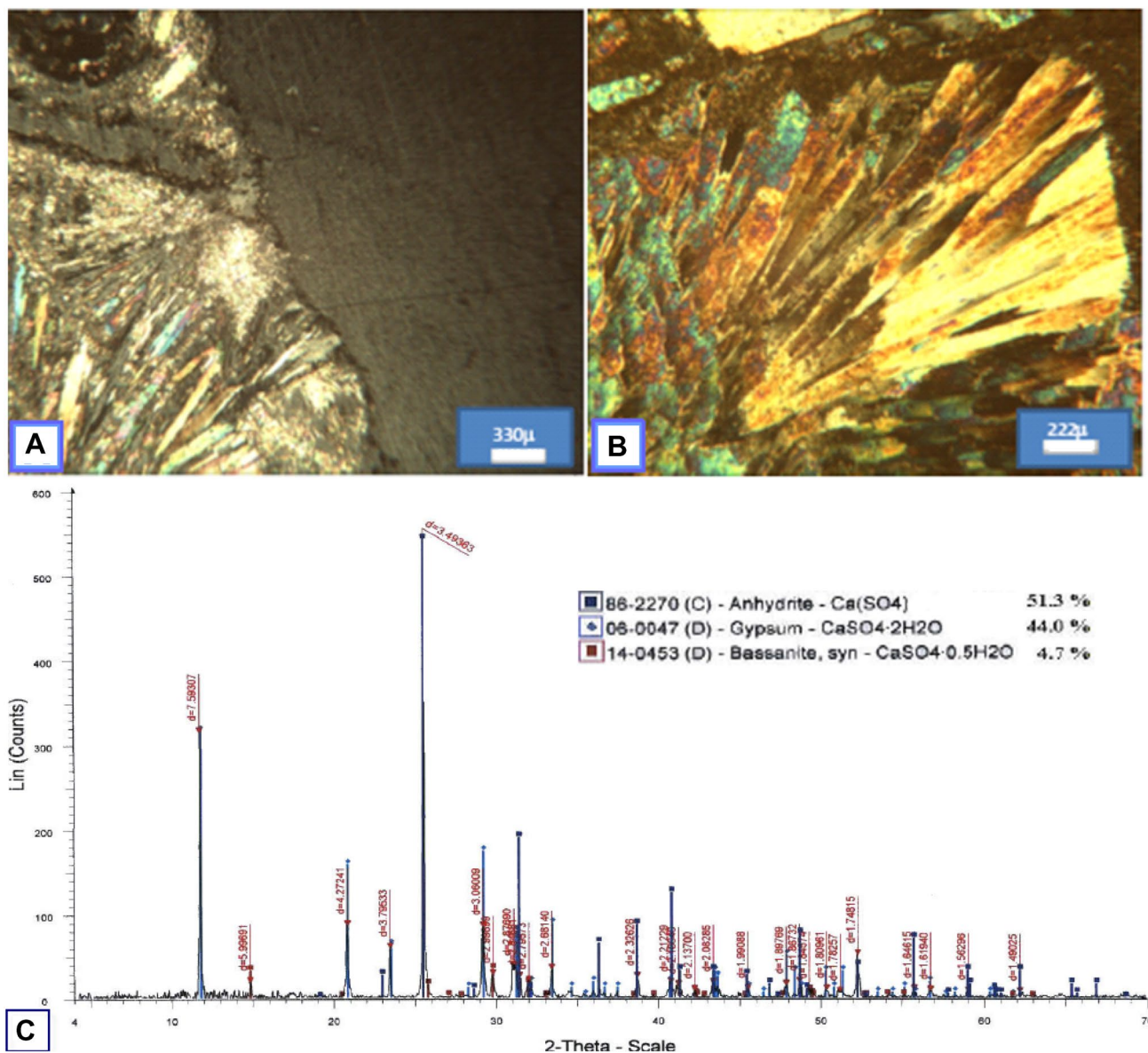
Fig. 4 Evaporitic microfacies of the South Gharib Formation: **A** Fine anhydrite phase (high interference colours) recrystallized into lath-shaped anhydrite replaced by gypsum (grey interference colours). Very coarse gypsum crystal filling the whole part of the right side of (dark grey interference colours) (between crossed Nicols, X30), Depth: 962.02 ft. **B** Palmate anhydrite crystals (lower left corner) which developed into rosette-like aggregates of lath-shaped anhydrite transformed partly into gypsum (grey interference colours) (between crossed Nicols, X45), Depth: 1040.08 ft. **C** The examined minerals through X-ray diffraction (XRD) Patterns, Depth: 962.02 ft

affected by several stages of evaporitic replacement. It is worth mentioning that most of the fossils and fossil fragments, as well as some of the carbonate clasts, show micritic coating (Fig. 5).

Calcareous claystone microfacies

These microfacies are represented by thin stringers separating the sulphate nodules at 962.02, 987.07, 995.00, and 1034.05 feet. It is composed of very finely crystalline to cryptocrystalline brownish-yellow undifferentiated clay minerals mixed with microcrystalline (micritic) calcite crystals which partly enclose the sulphate nodules. Minor scattered pyrite grains are observed (Fig. 6a). These microfacies show clear fracture porosity and inter-crystalline porosity type reached 3–5%.
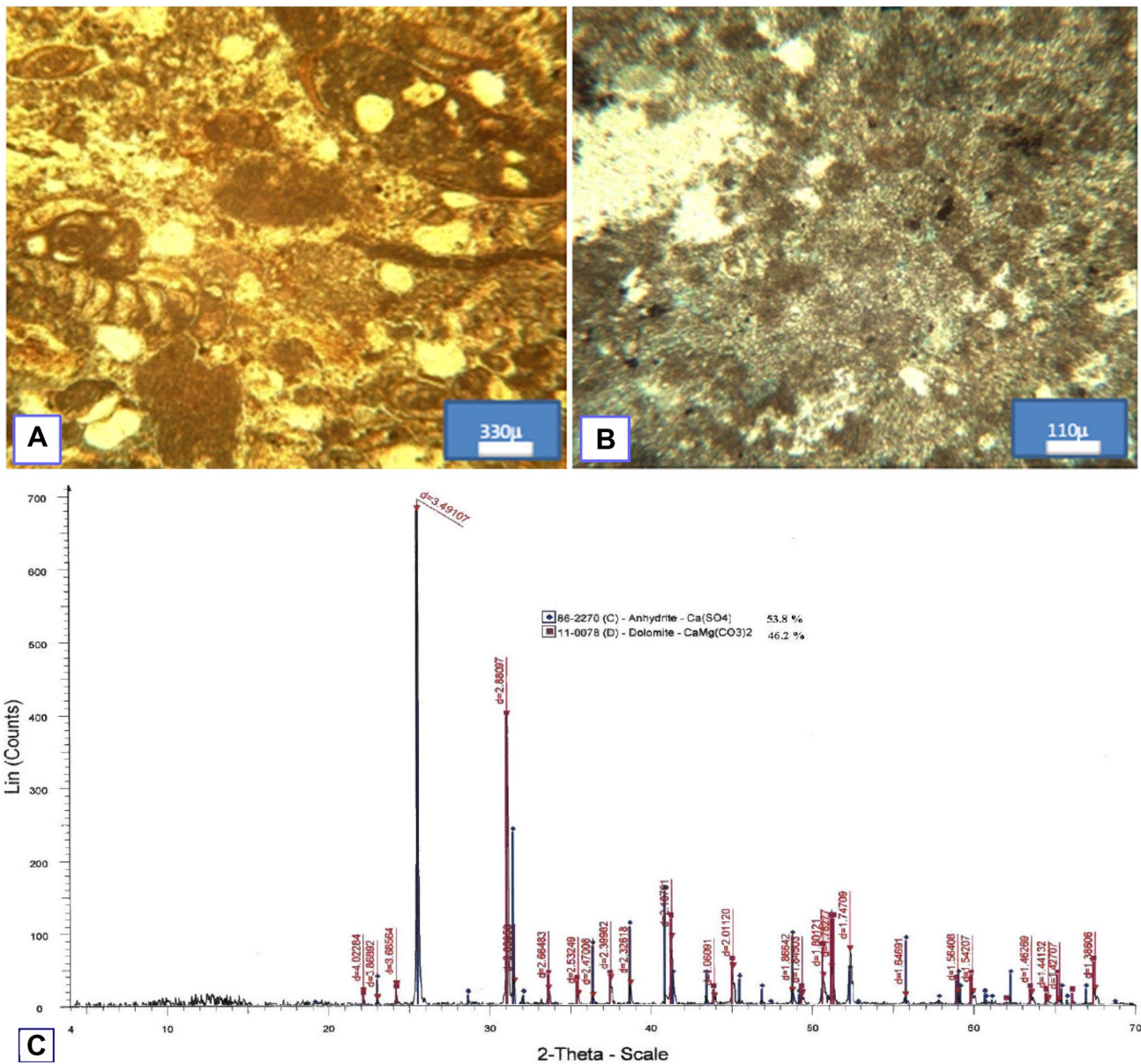
Fig. 5 Carbonates microfacies of the South Gharib Formation: **A** Partly silicified foraminiferal, intraclastic and bioclastic, embedded in argillaceous, microsparite (Plane Polarized Light, X45), Depth: 978. 10 ft. **B** Pelletal carbonate, partly replaced by evaporites. Note that the pellets are composed of microsparite (stained red), whereas the groundmass is composed of the dolomitic sprite (unstained). Note also the partly connected inter-crystalline pores (Blue Dye), (Plane Polarized Light, X90), Depth: 1011.08 ft. **C** The examined minerals through X-ray diffraction (XRD) Patterns, Depth: 1011.08 ft

Calcareous marls microfacies

It is represented by a thin band of marl (1.5–2.5 cm thick) enclosed between two sulphatized marly layers and thin stringers separating the sulphate nodules at depths of 874.09, 1028.05, 1031.11, and 1033.11 feet. The marl microfacies are represented either by yellowish-brown thin stringers calcareous marls separating the evaporitic nodules or by scattered remaining small corroded patches replaced by the evaporites. The thin sections investigation revealed interlaminated brownish-yellow calcareous marls with grey dolomitic micrite, sulphatized fine bioclasts, sulphatized micritic carbonate crystals, and cryptocrystalline to minutely crystalline undifferentiated clays. Separated lensoid evaporite nodules are developed mainly parallel to lamination, forming bird's eye structure. The local connected inter-crystalline porosity is created due to partly dolomitization of a few local patches into dolomicrite. This marl is rich in very fine bioclasts of a fraction of millimeters scale up to 0.7 mm. Many of

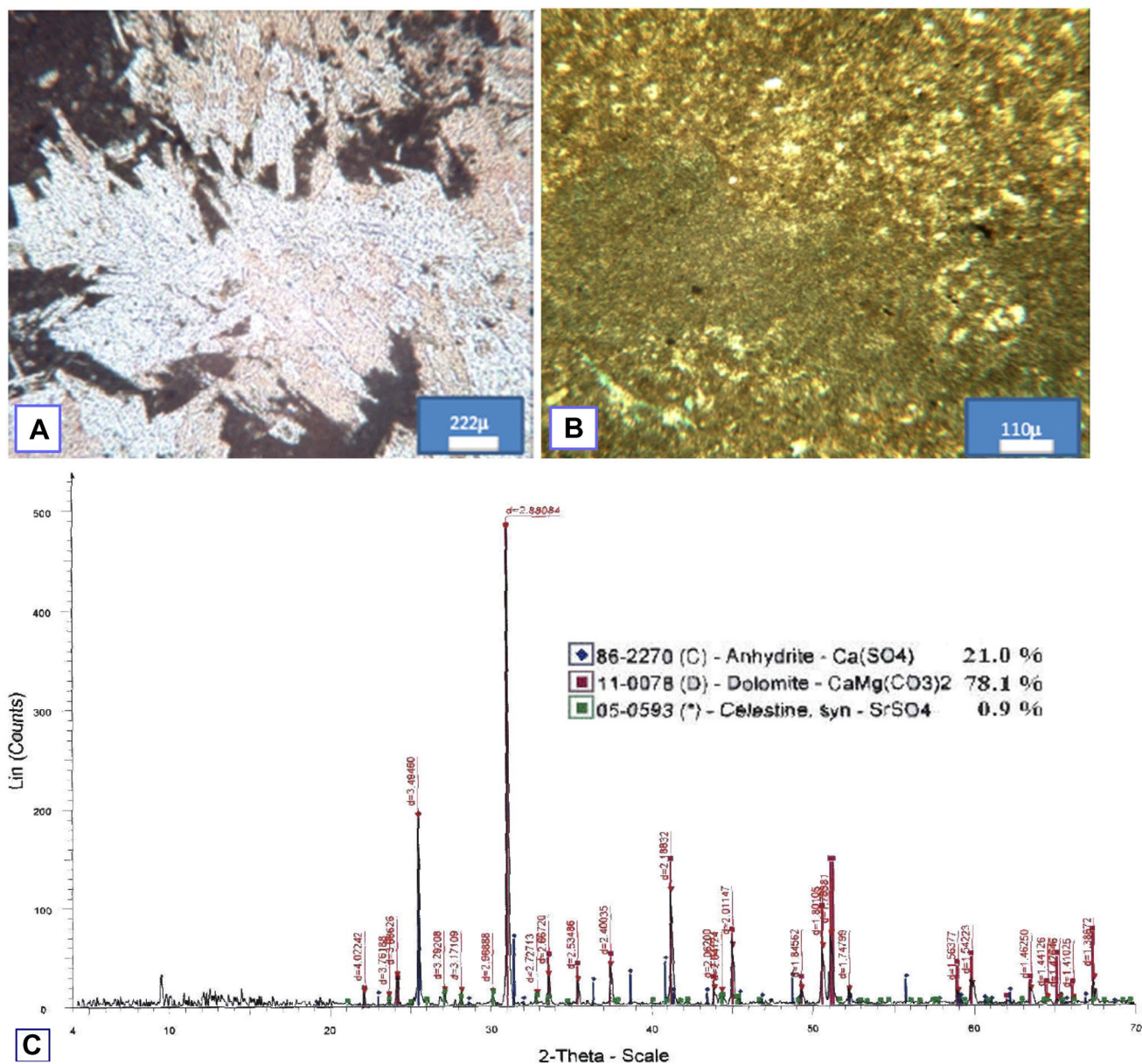**Fig. 6** Calcareous marls and clay microfacies of the South Gharib Formation: **A** Two phases of evaporitic minerals replacing dark calcareous claystone. The pink evaporite phase replaces the colourless anhydrite phase (Plane Polarized Light, X45), Depth: 995.00 ft. **B** Partly dolomitized marl with fine colourless bioclasts. Note that the dolomitic parts show a higher percentage of inter-crystalline porosity by Blue Dye (Plane Polarized Light, X90), Depth: 1031.11 ft. **C** The examined minerals through X-ray diffraction (XRD) Patterns, Depth: 1031.11 ft

these bioclasts are dissolved leaving disconnected moldic porosity (Fig. 6b, c). The marl band shows two stages of fracturing; an old one reached 0.5 mm wide and filled with evaporites and a later empty micro fracturing, partly cutting the old ones. The micro-fracture porosity type in the marl reaches 7%, and inter-crystalline porosity does not exceed 5%. Minor scattered fine pyrite grains are observed.

Vertical distribution of the evaporitic facies and their textures

Evaporitic microfacies are considered the most frequent microfacies in both cores 1 and 2. The observed evaporites textures of the studied cores of CSS-38 well can be determined as follow:

Syn-depositional evaporites (displacing and replacing)

It is worth mentioning that two main types of sulphate minerals (anhydrite and gypsum) of the studied section are the displacing and replacing syn-sedimentary evaporites as follow:

a. Lath-shaped anhydrite, developing, displacing, and breaking the earlier formed ones, as well as displacing and replacing the host sediments. By successive growth of new anhydrite laths, earlier formed laths rotate and break. Then, the result is a nodule with laths aligned margin sub-parallel to the nodule edge (Warren 2006). Such a type of lath-shaped anhydrite is present in most of the samples with variable percentages (Figs. 3b, 7).

b. Finely crystalline anhydrite, which constitutes the first stage of nodular development. Remains of such finely crystalline anhydrite are found in most of the samples, except the uppermost 19 feet of the section (Figs. 4a, 7).

c. Palmate anhydrite, which is recorded in a few samples of the deeper parts which are composed almost of entirely sulphate nodules (Figs. 4b, 7). Such a form of anhydrite is developed in the deeper parts of lagoons (Tucker 2001; Warren 2006).

d. Gypsum laths, found replacing anhydrite laths in almost all samples. This replacement was associated with the gradual shallowing of the region, possibly due to a gradual relative uplift (Tucker 2001; Fig. 8). The deeper parts reveal the reciprocal relationship of the lath-shaped
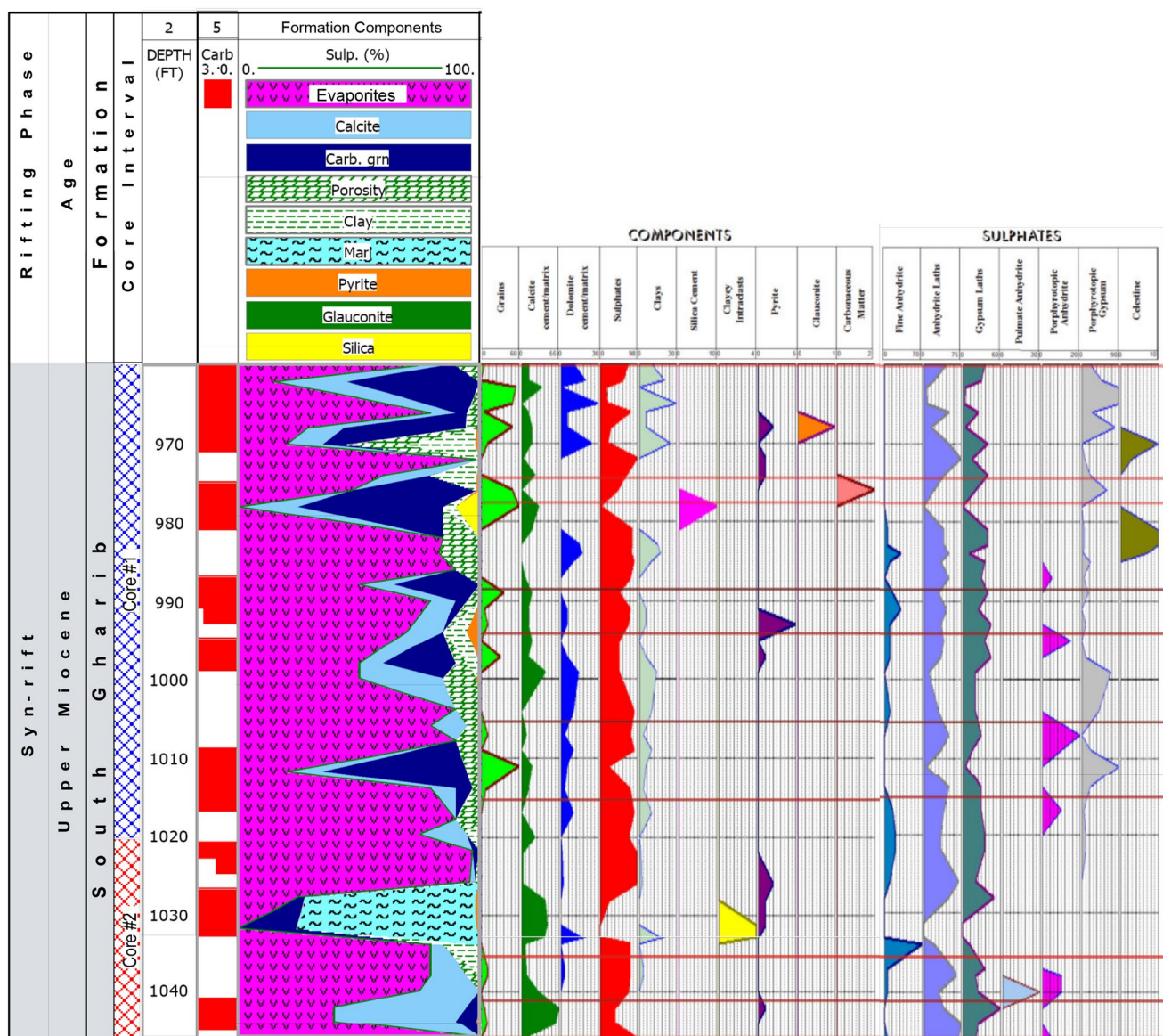

Fig. 7 Evaluated lithology of the studied South Gharib Formation based on Core analysis, Syn-rift Sediments of Gulf of Suez, Egypt
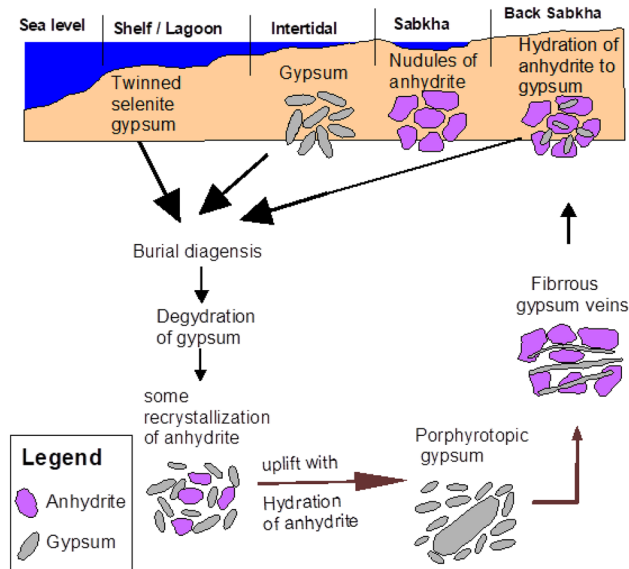
Fig. 8 The gypsum–anhydrite cycle shows mineral and texture changes from the surface into the subsurface and on uplifting (After Tucker, 2001)

gypsum and the lath-shaped anhydrite percentages. Both the two types of anhydrite laths and gypsum laths show lenticular twin complexes, and a rosette or rosette-like growth based on laboratory experiments (Figs. 4b, 7). Cody and Cody (1988) showed that such forms are developed by the increase in temperature and the increase in dissolved organic concentration. It is worth mentioning that the continuous growth of nodules and the development of evaporitic laths decrease greatly the porosity of the host rock. The occasionally observed low inter-crystalline porosity between the evaporitic laths becomes disconnected.

Post-depositional evaporites (secondary gypsum and anhydrite)

The post-depositional secondary evaporites include fibrous or coarsely crystalline, blade, gypsum, anhydrite, and celestite.

a. **Rosy fibrous gypsum**: Rosey fibrous gypsum occasionally replaces patches of all types of evaporites (whether anhydrite or gypsum). This is confined only to a few beds intercalating at depths (between 983.00 and 1017.03). The rosy colour could be due to a relatively higher content of iron (Fig. 3a). This simplifies Tucker's (2001) opinion about the possible formation of fibrous gypsum through the hydration of anhydrite during gradual uplift that will eventually develop Alabastrine gypsum (Fig. 8).

b. **Porphyrotopic gypsum and anhydrite:** Porphyrotopic gypsum and anhydrite result from a late diagenetic

sulphatization process that affected a great part of cores of CSS-38 well (Fig. 8). They are composed of coarse and blade crystals that occasionally enclose porphyritic crystals of the remaining non-replaced parts. This type of coarse evaporitic crystals largely occludes the different identified kinds of porosities. The porphyritic anhydrite affects largely the lower part and some beds in the rest part of the section. On the other hand, Fig. 7 shows that porphyritic gypsum is recorded with variable percentages in all samples (middle and upper part of the section). There is a reciprocal relationship between the percentages of porphyritic anhydrite and porphyritic gypsum (Figs. 4a, 7).

c. **Celestite:** According to Warren (2006), celestite is precipitated from calcium sulphate solution enriched pores spaces, which can be early occurred during evaporitic mudflat progradation when land derived meteoric waters flushed it. Then, strontium reacted with released sulphate ion within high intertidal and low intertidal-sub-tidal.

Celestite is recorded in the upper parts of the studied section (Fig. 7). They are present as anhedral to subhedral, medium crystalline mosaics. They are associated with the carbonates and marly beds of the upper supra-tidal cycles as well as the carbonate stringers between the evaporitic nodules of these cycles. The X-ray analysis proved the presence of such celestite (Fig. 3b).

The vertical distribution of carbonates grains

The vertical distribution of carbonate grains of the studied formation is mainly represented by bioclasts and pellets, and less commonly by intraclasts. Few samples enclose microbial laminae, forams, red algae, bryozoans, bivalves, gastropods, and alveolines; arranged in oscillatory abundance. Pellets and bioclasts are concentrated in 4 main, relatively narrow, intervals in the studied section, which are 960., 970.04, 989, 995.04, 1005.02, 1014.08, 1035, and 1040.08, where the lower three intervals are referring to shallow lagoonal intervals. The upper interval constitutes, also, show lagoonal intercalations in the upper parts of 4 sabkha cycles characterizing the top parts of the section. Bioclasts are additionally recorded in some other thin beds intercalating. Intraclasts partially constitute 3 beds only in core No. 1, which represent intertidal intervals. However, they reach about 40% of a bed forming a conglomeratic channel intercalating one of the sabkha cycles at the top parts of the studied section. Microbial laminae constitute two tidal beds, and red algae in one lagoonal bed of those beds intercalating the uppermost two sabkha cycles at the top of the studied section. Bivalves, gastropods, and alveolines are recorded in one sample at 1042.07 representing a shallow sub-tidal bed.

Interrelationship of the main components of the South Gharib Formation

The information about sedimentary and depositional environment evaluation is based mainly on vertical relative variation in their components of the studied section (Fig. 7), as Carbonate–Sulphates, Calcite–Dolomite and Gypsum–Anhydrite interrelationships as described briefly in the following:

Carbonate–Sulphate components interrelationships

The lithological components log represents the vertical variations in the carbonates and sulphates contents that were evaluated from the core and XRD analysis (Fig. 7). The calcite and dolomite, on one side, and the collective sulphate contents, on the other side, reflect a general reciprocal variation in percentages which points to a quiet understanding in the studied cores. It shows nodular and replacement of anhydrite and gypsum. Such kinds of sulphates that replace and displace carbonates, probably take place in the shallow sub-tidal, lagoonal, intertidal, and supra-tidal environments. However, few carbonate beds show no sulphate replacements at all. This particular part was most probably deposited in deeper parts of a lagoon and shallow sub-tidal environment (Tucker, 2001 and Warren, 2006).

Calcite–Dolomite components interrelationship

Carbonates are present in the groundmass in most of all the studied thin sections with variable percentages. Calcite is present up to 66% and dolomite up to 30% (thin sections). They also compose the carbonate grains occurring in certain horizons of cores. This is the normal result of the dolomitization diagenetic process accompanying sulphate deposition. Precipitation of gypsum is commonly associated with the dolomitization processes of carbonate rocks. This is the result of the increasing ratio of Mg/Ca and causes calcium ions to release, leading to more precipitation of gypsum (Tucker, 2001). Figure 7 shows a general upward decrease in dolomite percentages, especially in the uppermost part. This could be the result of the gradual shifting of environments toward supra-tidal environments, especially in the upper part of the studied section.

Gypsum–Anhydrite components interrelationship

The vertical variations of the different sulphate types identified (thin sections) are represented in Fig. 7. Gypsum and anhydrite are generally represented by nearly equal distribution and with possible parallel variation in content in most samples of the upper core No. 1 (Fig. 7). Anhydrite is deposited in the landward parts of the sabkhas as layers or thin beds of coalesced nodules. These beds commonly are irregularly buckled and contorted, forming what so-called enterolithic texture. Very arid regions with intense solar heating at the surface can dehydrate gypsum into bassanite/anhydrite. Gypsum may convert, also, into anhydrite in the evaporitic mudflats and capillary zones of sabkhas, where gypsum is bathed in highly saline NaCl brines (Warren, 2006). By increasing the concentration of pore fluids across the Sabkhas, the gypsum crystals are replaced by a fine mush of equal and lath-shaped anhydrite crystals. In the most landward part of the Sabkha, rehydration of anhydrite to gypsum may occur from contact with fresh continental groundwater. The seasonal temperatures exceed 35º C, and arid climate with high mean annual temperatures (more than 22º C) is the main factors required for the anhydrite presence (Tucker, 2001).

General downward increase in anhydrite and decrease in gypsum contents, besides more replacements of anhydrite laths, by gypsum laths in the upper parts of the samples, can be noticed in section (Fig. 7). This meets with the result of the burial to depths greater than several hundred metres; all $CaSO_4$ is present as anhydrite, by uplifting. Anhydrite is normally converted to secondary gypsum. The anhydrite–gypsum replacement was most probably associated with the gradual shallowing of the region, possibly due to a gradual relative uplift (Tucker, 2001) (Fig. 8).

Environmental zonation of the South Gharib Formation

The following zonation of the sedimentary environment could be evaluated and summarized, from base to top (Fig. 9) as:

Shallow sub-tidal (1045.10–1040.08)

Characterized by relatively more calcite than dolomite, with some sulphatization. It is relatively rich in bivalves and has much fewer bioclasts, gastropods, alveolines, and benthic forams. Rare pyrite grains are also recorded (Fig. 9).

Shallow lagoonal (1040.08–1035.00)

Rich in evaporitic nodules which enclose carbonate stringers in between. These stringers are relatively rich pellets but with few bioclasts and red algae. The evaporites include relatively more anhydrite than gypsum. Some porphyritic anhydrite is also recorded (Fig. 9).

Intertidal (1035.00–1014.08)

Devoid of carbonate grains, except a few bioclasts mingled with clayey intraclasts in two basal samples. These particular
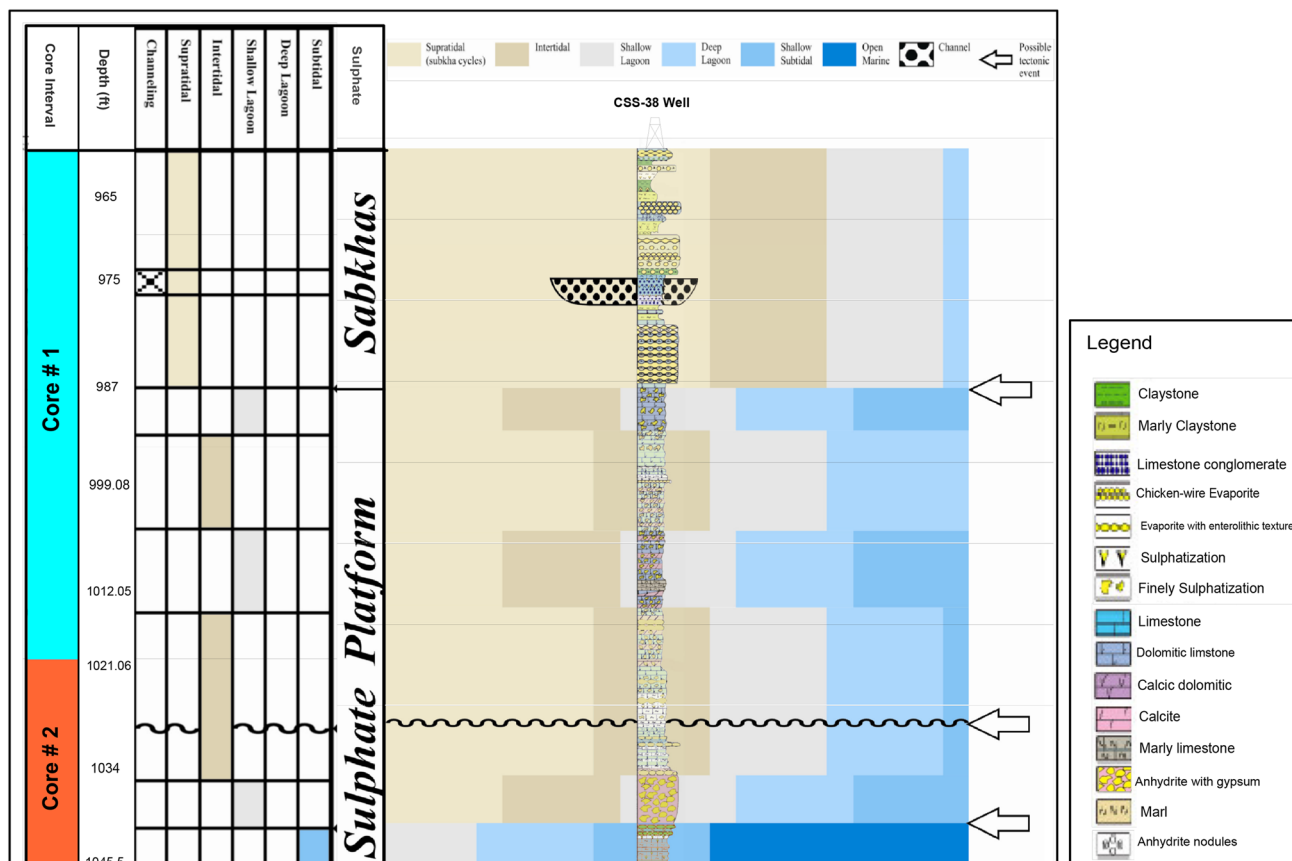
Fig. 9 The interpretative diagram of Migration and vertical development of sedimentary environments of the South Gharib Formation, Syn-rift Sediments of Gulf of Suez, Egypt

samples are almost devoid of evaporites, but the rest of the interval is relatively rich in anhydrite and gypsum, which go almost parallel in their frequency variations. The top parts of this interval show some porphyrotopic anhydrite and gypsum as well. Clayey ingredients are also represented in some marly beds. Rare pyrite is recorded in some samples in the middle parts of this interval. A brecciated bed could either point to seismic activity or a temporal exposure (Fig. 9).

Shallow lagoonal (1014.08–1005.08)

This interval is similar in its characteristics to the previously described shallow lagoonal one. It only differs in its relatively higher marly as well as porphyrotopic anhydrite and gypsum contents (Fig. 9).

Intertidal (1005.08–995.04)

Similar in its characteristics to the previously described intertidal one. It only differs in its relatively higher bioclastic and intraclastic content in one of the beds, as well as

relatively higher porphyrotopic gypsum and some porphyrotopic anhydrite contents (Fig. 9).

Shallow lagoonal (995.04–989.00)

Similar in its characteristics to the previously described two shallow lagoonal intervals. It only differs in its relatively higher bioclastic content as well as in the presence of relatively lower porphyritic gypsum content, as the only porphyritic secondary evaporitic phase present (Fig. 9).

Supra-tidal Sabkha cycles (989.00–960.00)

Four sabkha cycles could be identified in this interval. Although each cycle starts at its base by shallow lagoonal to intertidal carbonate sediments, yet, and due to the dominance of evaporites at the top of each cycle, they are collectively described here as four sabkha cycles deposited in a supra-tidal environment. These cycles are characterized by the upward increase in the clay content in the form of more marly content. The upward increase

Migration and vertical development of sedimentary environments of the south Gharib Formation

Based on the core examination, vertical development of sedimentary environments of the studied formation can be differentiated into three phases which are:

- First; the earliest relatively deeper phase between depths 1066.00—1040.08 ft where shallow sub-tidal fossiliferous carbonates and marly carbonates have prevailed.
- Secondary; is the intermediate oscillatory phase between depths 1040.00 and 989.00 ft, characterized by carbonate deposits of variable composition rich in nodular evaporites.
- The latter is occasionally developed largely leaving carbonate stringers of the host rock in between. The latest is uplifted shallower phase between depths 989.00–966.00 ft which is supra-tidal environment prevailed depositing 4 thinning upward sabkha cycles. Each cycle started at the base by thin sulphatized intertidal to shallow lagoonal carbonates and marly carbonates and ended by relatively thicker supra-tidal nodular evaporites showing extensive enterolithic and chicken wire structures which enclosing thin stringers of the host rock (Fig. 9).

In porphyritic gypsum, the presence of few samples of celestite, and the presence of a carbonate fine conglomeratic channel (Fig. 9).

Depositional model of the south Gharib Formation

One important additional control that can lead to the repetition of the cycles is eustatic sea-level change (Tucker, 2001). In addition, sediments type is a function of water depth during sedimentation and the distance from the basin margin (Hagras, 1976). When the global sea level is high relative to the intracratonic basin, open-marine carbonates are deposited therein marginal platforms and on the basin floor, with a moderate fall, so that there is still some connection with the open ocean. Evaporites will be precipitated in the restricted basin, mainly around the shallow basin margins. Selenitic gypsum platforms with sabkhas behind are likely to be formed at this stage and euxinic carbonates will be deposited in the basin centre. With a more drastic sea-level fall, the basin is cut off, laminated anhydrite and halite will be precipitated in the basin centre. Periodic replenishment of the water body will allow a thick succession to develop, but if this does not occur, saline pans and sabkhas will be present on the desiccated basin floor. A subsequent major sea-level rise will re-establish the open-marine conditions in the basin and strata's new cycle.

Figure 10 represents Tucker's (2001) model, which is adopted to explain the depositional history of the studied cores of well CSS-38. Intermediate sea levels are dominated due to partial closure of Gulf of Suez, which caused first the deposition of the lowermost deep lagoonal and shallow 'subtidal' phase as well as the intermediate 'intertidal-shallow lagoonal oscillatory phase'. These two phases are equivalent to the 'sulphate platform' part in Tucker's model, before the culmination of deposition by the supra-tidal (Sabkha)

Fig. 10 Evaporite deposition Model in an intracratonic basin, where eustatic see-level (S. L.) changes have major control
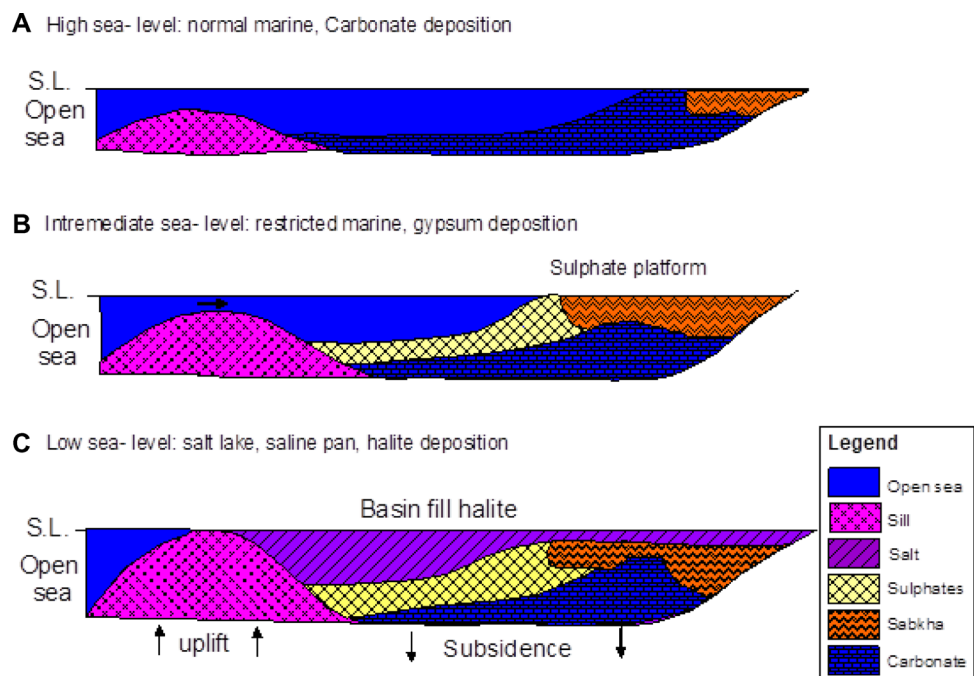
phase. By further lowering of sea level, all these phases are developed into the proper thick basin-fill evaporite of Ras Gharib Formation in more basinal areas of Gulf of Suez. It is believed that during the deposition of South Gharib and Zeit Formations in the Gulf of Suez tectonics played a great role in the restriction of the Gulf of Suez rather than lowering of sea level (Orszag-Sperber et al. 1993).

Discussion of Petrophysical and electrical properties

Petrophysical properties

The percentage of the measured volume of pore space or void V_p (cm^3) to the total sample volume V_b (cm^3) is known as porosity (φ).

$$\varphi = \frac{V_p}{V_b} \tag{6}$$

where the bulk density σ_b values are the contribution of both grain and pore phases. The following formula was used to compute bulk density (σ_b, g/cm^3):

$$\sigma_b = W_d / V_b \tag{7}$$

where the dry sample weight W_d (g) and grain density σ_g (g/cm^3) are as follows:

$$\sigma_g = W_d / V_g \tag{8}$$

where V_g is the volume of grain (cm^3).

$$V_g = V_b - V_p \tag{9}$$

A gas permeameter filled with nitrogen gas was used to test gas permeability (K, in mD):

$$K = Q\mu L / (A\Delta P) \tag{10}$$

where Q is the flow rate (cm^3/s), μ is the viscosity of the fluid (centipoises), ΔP is denoted by the pressure gradient (atm./cm), A is the cross-sectional area of the sample (cm^2), and L is the sample length (cm).

The bulk density depends on porosity φ with a highly reliable relationship ($R^2 = -0.9976$, Fig. 11). Bulk density is calculated using:

$$\phi = 2.698 - 0.0363\sigma_b (R^2 = -0.9976) \tag{11}$$

The values of the permeability (k) are mostly ranked as fair to excellent for the studied samples. The values range from 0.4 mD (for low values) to 958.66 mD (for high values). Figure 12 shows the plotted values of permeability
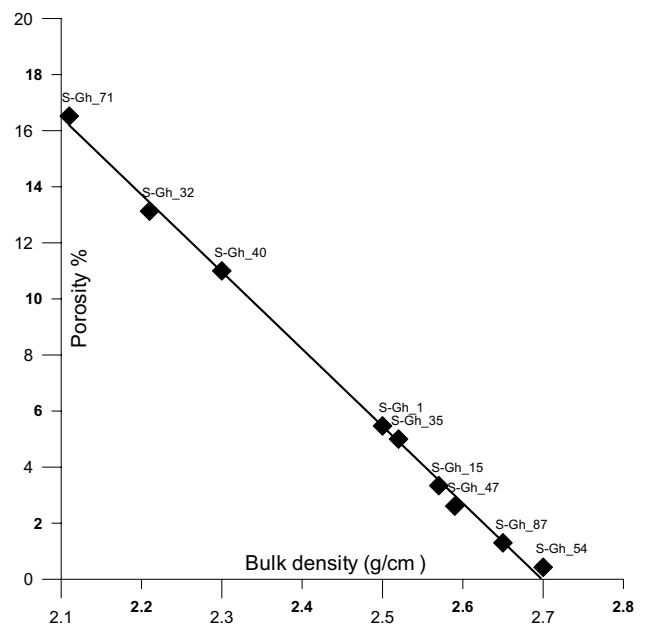
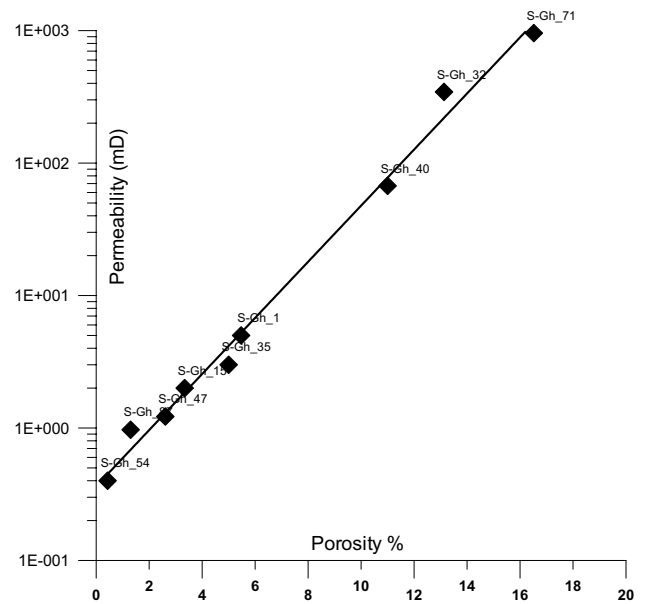**Fig. 11** The relationship between porosity and bulk density

Fig. 12 The relationship between permeability and porosity

against the porosity measured using the helium method. It is mostly dependent on porosity with a more reliable relationship with porosity. The regression equation calculated for these relations is:

$$k = 0.1031 \, e^{0.53\varphi} \quad (R^2 = 0.91) \tag{12}$$

Electrical properties

Low-frequency dispersion dominates the frequency response of electrical characteristics. In the frequency range of 10 Hz to 100 kHz, the change of AC electrical characteristics has been researched and analysed (room temperature). The relative permittivity is shown against frequency in Fig. 13. Due to polarization, dielectric constant (ε') values at high frequencies have been almost frequency independent and decrease with increasing frequency. Because beyond a certain frequency, the hopping of electrons cannot follow the applied alternating field (Chelidze and Gueguen 1999), i.e. the electrons' velocity cannot follow the applied field's speed, relative permittivity values decrease with frequency rise, then stabilize. The increase in void lengths between grains, i.e. increasing the pore spaces between the conducting mineral surfaces, causes a progressive drop in relative permittivity as the overall concentration of conductor decreases. With a reduction in frequency or a rise in whole conductor concentration, the capacitance gradually increases (Chelidze et al. 1999). The frequency dependency of the dielectric constant (ε') can be ascribed to Maxwell–Wagner polarization, in which heterogeneity in rocks causes the dielectric constant (ε') to vary with frequency. Charge transports are gathered at conducting grain margins due to heterogeneity, resulting in interfacial polarization. The variation of relative dielectric constant with frequency has shown essentially identical behaviour for all samples, showing that they follow the same power-law (Jonscher 1999). Furthermore, the behaviour of dielectric constant dispersion is connected to the use of a field that allows electrons to hop between two distinct places inside the atoms. This also increases the electrical component's resistance to dielectric constant change. Because the charge carriers are unable to follow the rotation of the electric field at high frequencies, their fluctuation or rotation begins to delay behind the applied field, resulting in a drop in the dielectric constant. The sample with the highest relative permittivity (lowest porosity) is S-Gh_1, whereas the sample with the lowest value is S-Gh_32 (may be due to texture, Fig. 13).

The conductivity versus frequency across all specimens is shown in Fig. 14. In general, conductivity rises as frequency and overall conductor concentration rise (Levitskaya and Sternberg 1996a, b). Because of the randomness and heterogeneity in the samples, the overall rise in conductivity is not ordered. For certain samples (S-Gh_1, S-Gh_35 and S-Gh_54, and S-Gh_71), there is just one slope with frequency, whereas for others (S-Gh_15, S- S-Gh_32, Gh_40, S-Gh_47, and S-Gh_87), there are two slopes with frequency (texture effect). The conductivity is low and almost flat at relatively low frequencies (for samples of two slopes). At higher frequencies, conductivity rises owing to the development of more continuous conduction channels (Knight 1983; Levitskaya and Sternberg 2000). Particles are encouraged to overcome energy level barriers to create continuous current channels as frequency increases, and as a result, conductivity rises (Jonscher 1999; Gomaa and Elsayed 2009; Gomaa et al. 2009). As frequency grows, particles are urged to overcome energy level barriers to generate continuous current channels, and conductivity rises as a result (Jonscher 1999; Gomaa et al. 2015, 2009). The conductivity characteristic (almost) follows a power law with frequency (ω),
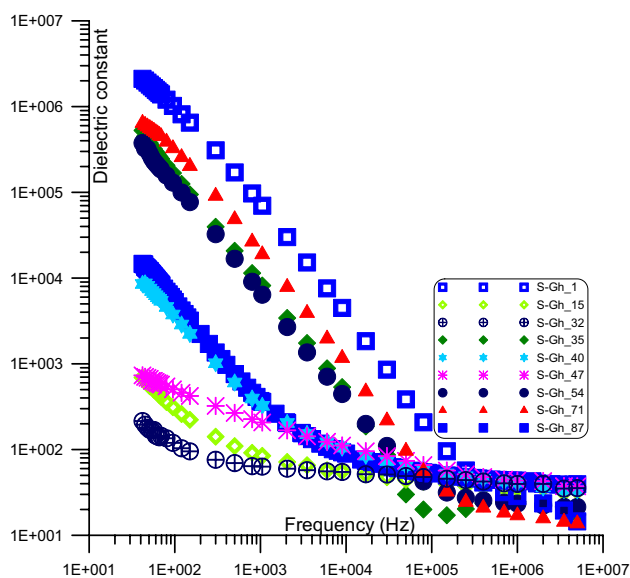
$$\sigma \propto \omega^n \tag{13}$$

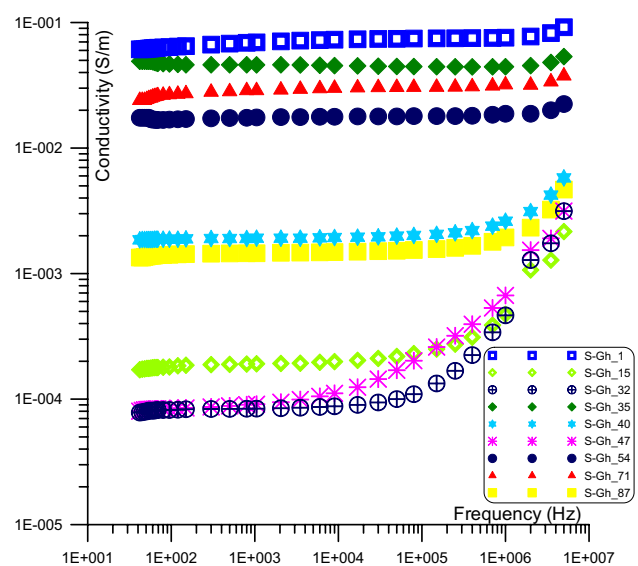**Fig. 13** The dielectric constant as a function of frequency for samples

Fig. 14 The conductivity as a function of frequency for samples

For samples with one slope, n is the curve slope (∼ 0.0). DC conduction might be the cause of the low-frequency slope (conducting elements). High conductivity samples include S-Gh_1, S-Gh_35, S-Gh_54, and S-Gh_71, whereas low conductivity samples include S-Gh_15, S-Gh_32, Gh_40, S-Gh_47, and S-Gh_87 (Fig. 14).

Conductivity's frequency dependency is a result of polarization effects. An analogy between specimens and the electrical equivalent circuit may be created by assuming a capacitance between conductor grains. Conductivity is mostly impacted by conducting links when the concentration of conductor grains is high. The conductivity of the samples will not change considerably up to a specific frequency. Above that frequency, the contribution of the capacitor (insulator grains) is enormous. Few conducting grain linkages may be detected mostly around the percolation threshold, and the air gap (capacitors) impact among conductor grains begins to be quite large (Efros and Shklovskii 1976). The power in gabs (capacitors) increases as the frequency increases, and the overall conductivity increases as a result (Song et al. 1986).

Diffusion inside clusters influences both the frequency dependence of conductivity (above P_C) and the polarization effects between semiconducting grains (Knight 1983; Knight and Endres 1990). For the most majority, the conductivity exhibits a flat response throughout the frequency range. This is because, in an electric field, electrons are free to flow over long distances. Electrons can go through various and distinct channels in the infinite clusters for highly conducting samples (S-Gh_1, S-Gh_35, S-Gh_54, and S-Gh_71). Only a few percolating pathways exist around critical concentration, and electron movement in the limited channels is extremely important, and the conduction mechanism will grow with frequency.

Conductivity values are determined by the polarization and flow of electrons in conducting channels in the region below P_C. Finally, when the frequency rises, conductivity rises as well. The formula $\sigma \propto \omega^2$ will be applied to samples below the percolation P_C area. The polarization between isolated conducting grains is responsible for the energy wasted at low frequencies.

There is a consistent transition from ω^n to ω^2 behaviour near the percolation threshold P_C (Levitskaya and Sternberg 1996a, b; Levitskaya and Sternberg 2000). The asymptotic is not apparent (> 100 Hz) even for samples approaching the percolation threshold P_C (Fig. 14).

Figure 15 shows a description of complex impedance. In most cases, there is a line attached to a semicircle in the impedance diagram that represents the relatively high conduction in the samples. The size of the arc (the portion of the semicircle) decreases when the critical beak frequency changes (with the change of the total conductor concentration in the samples). Relatively large conductor concentrations, the critical beak frequency moves to higher frequencies as the total conductor concentration increases in samples S-Gh_1, S-Gh_35, S-Gh_54, and S-Gh_71 (Ruffet et al. 1991a, b). Case studies S-Gh_15, S-Gh_32, Gh 40, S-Gh_47, and S-Gh_87 show a semicircle attached to a tiny arc, whereas samples S-Gh_1, S-Gh_35, S-Gh_54, and S-Gh_71 show two semicircles attached (bulk semicircle at high frequency and interface semicircle at low frequency). The critical beak frequency is the frequency that divides the two semicircles, and its value rises as the overall conductor concentration in the sample rises. The distances between conducting grains reduce as the conductor increases until the percolation threshold is reached, during which the curve's distinctive look changes from a line to an arc, and finally to a semicircle.

Because the insulating gaps between conducting grains shrink as overall conductor concentration rises, the dielectric constant rises. Up until the first continuous conductor channel is produced, the gaps between conducting grains diminish. The total conductor concentration was found to be over the critical concentration in the majority of the samples (S-Gh_1, S-Gh_35, S-Gh_54, and S-Gh_71). As the overall conductor concentration rises, the number of continuous channels of conductor grains between electrodes grows at the cost of insulator routes, and the conductivity rises with it (Table 1).

Figure 16 shows the phase angle as a function of frequency. Also, there are two groups of samples S-Gh_1, S-Gh_35, S-Gh_54, and S-Gh_71 for high conductor concentration and S-Gh_15, S-Gh_32, Gh 40, S-Gh_47, and S-Gh_87 for low conductor concentration. When the distances between conducting grains are extremely large then the dielectric constant does not change with increasing conductor concentration, and accordingly decreasing insulating distances, below the percolation threshold. At this stage, the dielectric constant changes, slightly, with increasing conductor concentration. The dielectric constant abruptly increases near the percolation threshold due to the abrupt shrinkage of the distances between conducting grains becoming very short. Because certain conducting grains and conducting clusters touch each other (insulating distances between conducting grains diminish) over the percolation threshold, the dielectric constant begins to decline again (Gomaa 2014). The conductivity displays a minor rise at low conductor concentrations below the percolation threshold (and with the growth of conductor concentration), followed by a sudden increase in conductivity at the percolation threshold. After the percolation threshold, the conductivity continues to display a minor rise with the mutual increase in the conductor concentration. Even if they have the same concentration and composition of substances, the structure and interconnections between grains or elements in samples might differ
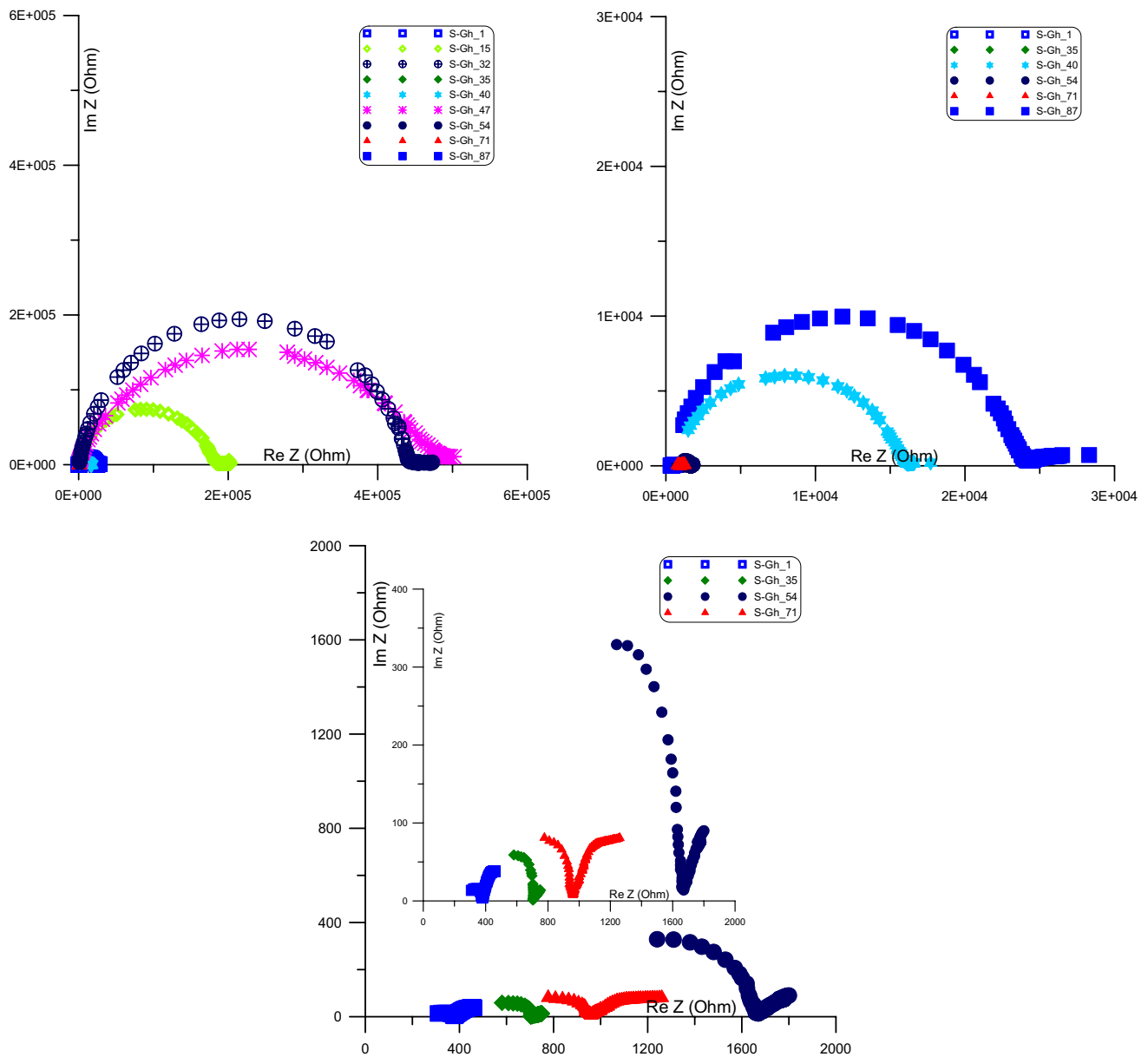
Fig. 15 The impedance plane of samples as a function of frequency

Table 1 Petrophysical parameters of sandstone samples

| Sample No	Porosity %, (Helium)	Bulk Density g/cm³	Grain Density g/cm³	Permeability, mD	Silt and Clay %	Sand %	Carbonate %	Formation
S-Gh_1	5.47	2.5	2.65	5	8.6	73.6	17.8	South Gharib
S-Gh_15	3.34	2.57	2.66	2	7.9	59.3	32.8	South Gharib
S-Gh_32	13.13	2.21	2.61	344.55	1	96.5	2.5	South Gharib
S-Gh_35	5	2.52	2.71	3	9.7	68.4	21.9	South Gharib
S-Gh_40	11	2.3	2.61	67.31	3.9	89.3	6.8	South Gharib
S-Gh_47	2.61	2.59	2.62	1.22	6.2	89.3	4.5	South Gharib
S-Gh_54	0.43	2.7	2.72	0.4	7.4	56.9	35.7	South Gharib
S-Gh_71	16.52	2.11	2.59	958.66	3.6	90.1	6.3	South Gharib
S-Gh_87	1.3	2.65	2.61	0.97	9.6	56.3	34.1	South Gharib
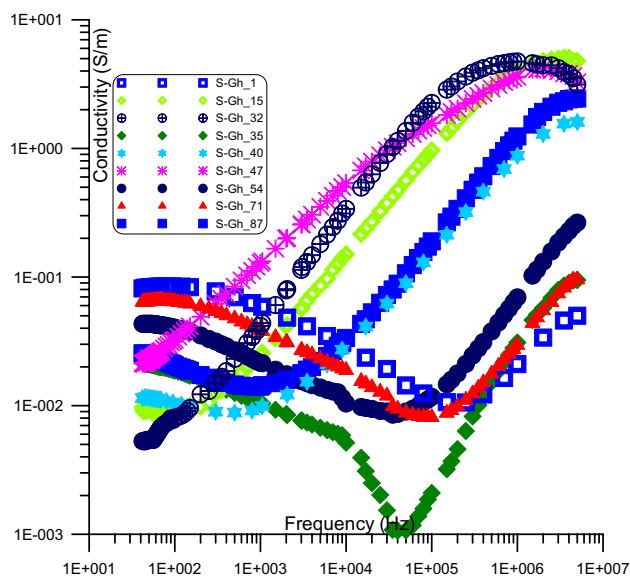
Fig. 16 Shows the phase angle of samples as a function of frequency

significantly (Sen 1981; Olhoeft 1985; Abou El-Anwar and Gomaa, 2013).

The current spectrum of electrical characteristics has the advantage of providing enormously long and comprehensive information about each sample. The limitations of the electrical properties spectrum are that there are various materials with the same resistivity, many characteristics that influence the resistivity of the samples, and also that the texture of each type of sample is different.

Summary and Conclusion

The analysis of core samples reveals that:

- The South Gharib Formation is mostly composed of sulphate, grading progressively into sulphate-rich beds in the upper section with little carbonates intercalation.
- Laminated dolomitic limestone with evaporite, sloping gradually into laminated dolomitic limestone and marly limestone in the bottom portion.
- Patchy oil staining was detected in the thin streaks and basal laminated dolomitic limestone, which do not have good petrophysical parameters.
- Comprehensive three-dimensional facies and diagenetic variations, in addition to the porosity and permeability variations that characterise the syn-rift sediments of the south Gharib Formation, are suggested to be done in the surrounding area of well CSS-38.

- Three probable tectonic events during the South Gharib Formation's deposition might be examined at 1040.08, 1028.09, and 987 feet. It might be a sign of seismic activity or of a temporal exposure.
- Electrical characterization was performed at frequencies ranging from 10 Hz to 100 kHz, and the relationship between mineral composition (surface and subsurface) and electrical properties (conductivity, permittivity, and impedance) was discussed.
- The majority of the hand specimen samples were porous of high porosity.
- Depositional processes (cementation, compaction, and the formation of authigenic minerals) control porosity by reducing pore spaces dramatically.
- Minor variations in electrical results may be caused by variations in grain arrangement and interactions between grains or components in samples.
- An increase in total conductor concentration is referred to as an increase in dielectric constant.
- The bulk of the samples should have been below the critical concentration, but some should have above the percolation threshold. A variety of factors can be combined to get the same electrical performance.

Data availability The authors confirm that the data supporting the findings of this study are available within the article.

Declarations

Conflict of interest On behalf of all authors, the corresponding author states that there is no conflict of interest.

References

Abou E-A, Gomaa MM (2013) Electrical properties and geochemistry of carbonate rocks from the Qasr El-Sagha formation El-Faiyum, Egypt. Geophys Prospect 61:630–644

Abul-Nasr RA (1990) Re-evaluation of the Upper Eocene rock units in west central Sinai Egypt, Ain Shams University. Earth Sci Ser 4:234–247

Anees A, Zhang H, Ashraf U, Wang R, Liu K, Abbas A, Ullah Z, Zhang X, Duan L, Liu F, Zhang Y, Tan S, Shi W (2022a) Sedimentary facies controls for reservoir quality prediction of lower Shihezi member-1 of the Hangjinqi Area. Ordos Basin Miner 12:126. https://doi.org/10.3390/min12020126

Anees A, Zhang H, Ashraf U, Wang R, Liu K, Mangi HN, Shi W (2022b) Identification of favorable zones of gas accumulation via fault distribution and sedimentary facies: insights from Hangjinqi area, northern Ordos basin. Front Earth Sci 9:1375. https://doi.org/10.3389/feart.2021.822670

Ashraf U, Zhu P, Yasin Q, Anees A, Imraz M, Mangi HN, Shakeel S (2019) Classification of reservoir facies using well log and 3D seismic attributes for prospect evaluation and field development: a case study of Sawan gas field, Pakistan. J Petrol Sci Eng 175:338–351

Ashraf U, Zhang H, Anees A, Mangi HN, Ali M, Zhang X, Tan S (2021) A core logging, machine learning and geostatistical modeling interactive approach for subsurface imaging of lenticular geobodies in a clastic depositional system, SE Pakistan. Nat Resour Res 30(3):2807–2830

Bakr MMY, Wilkes H (2002) The influence of facies and depositional environment on the occurrence and distribution of carbazoles and benzocarbazoles in crude oils: a case study from the Gulf of Suez. Egypt Org Geochem 33(2002):561–580

Chelidze T, Gueguen Y (1999) Electrical spectroscopy of porous rocks: a review -I. Theoretical models. Geophys J Int 137:1–15

Chelidze T, Gueguen Y, Ruffet C (1999) Electrical spectroscopy of porous rocks: a review II. Experimental results and interpretation. Geophys J Int 137:16–34

Chew WC, Kong JA (1980) Effects of fringing fields on the capacitance of circular microstrip disk. IEEE Trans Microwave Theory Tech 28(2):98–104

Choquette PW, Pray LC (1970) Geologic nomenclature and classification of porosity in sedimentary carbonates. Am Asso Petrol Geol Bull 54(2):207–250

Cody RD, Cody AM (1988) Gypsum nucleation and crystal morphology in analog saline terrestial envioronments. J Sed Petrol 58:247–255

Corex (2009) Special core analysis study, Issaran Field, Egypt. Internal reports

Dunham RJ (1962) Classification of carbonate rocks according to depositional texture: In Ham WE (ed) Classification of carbonate rocks: American Association of Petroleum Geologists, Memoir vol 1, pp 108–121

Efros AL, Shklovskii BI (1976) Critical behavior of conductivity and dielectric constant near the metal–non-metal transition threshold. Phys Status Sol 76:475–489

EGPC (Egyptian General Petroleum Corporation) (1996) Gulf of Suez oil and gas fields, A comprehensive overview. Cairo, Egypt, pp 520–528

El-Ghali MAK, El Khoriby E, Mansurbeg H, Morad S, Ogle N (2013) Distribution of carbonate cements within depositional facies and sequence stratigraphic framework of shore face and deltaic arenites, lower Miocene, the Gulf of Suez rift, Egypt, Marine and Petroleum Geology

Embry AF, Klovan JE (1971) A late devonian reef tract on northeastern Banks Island, NWT: Canadian Petroleum Geology Bulletin, vol 19, pp 730–781

Evans AL (1988a) Neogene tectonic and stratigraphic events in the Gulf of Suez Rift area, Egypt. Tectonophysics 153:235–247

Evans AL (1988b) Neogene tectonic and stratigraphic events in the Gulf of Suez rift area. Egypt Tectonophys 153:235–247

Folk RL (1959) Practical petrographic classification of limestones: American Association of Petroleum Geologists Bulletin, vol 43, pp 1–38

Folk RL (1962) Spectral subdivision of limestone types: In Ham WE (ed) Classification of carbonate rocks, American Association of Petroleum Geologists, Memoir vol 1, pp 62–84

Gomaa MM (2008) Relation between electric properties and water saturation for hematitic sandstone with frequency. Ann Geophys 51(5/6):801–811

Gomaa MM (2009) Saturation effect on electrical properties of hematitic sandstone in the audio frequency range using nonpolarizing electrodes. Geophys Prospect 57:1091–1100

Gomaa MM (2013) Forward and inverse modeling of the electrical properties of magnetite intruded by magma Egypt. Geophys J Int 194(3):1527–1540

Gomaa MM, Alikaj P (2010) Effect of electrode contact impedance on AC electrical properties of wet hematite sample. Marine Geophys Res 30(4):265–276. https://doi.org/10.1007/s11001-010-9092-y

Gomaa MM, Elsayed M (2009) Thermal effect of magma intrusion on electrical properties of magnetic rocks from hamamat sediments NE Desert, Egypt. Geophys Prospect 57(1):141–149

Gomaa MM, Shaltout A, Boshta M (2009) Electrical properties and mineralogical investigation of Egyptian iron ore deposits. Mater Chem Phys 114(1):313–318

Gomaa MM, Kassab MA, El-Sayed NA (2015) Study of petrographical and electrical properties of some Jurassic carbonate rocks, north Sinai. Egypt Egypt J Petrol 24:343–352

Hagras M (1976) Some geological observations in the Gulf of Suez area, Egypt. In: 8th petroleum exploration and production conference, EGPC, Cairo, Egypt, pp 53–73

James NP (1984) Shallowing-upward sequences in carbonates. In: Walker RG (ed) Facies models, geological association of Canada, Geoscience Canada, Reprint Series 1, pp 213–228

Jonscher A (1999) Dielectric relaxation in solids. J Phys D Appl Phys 32:R57–R70

Khalil B, Mesheref WM (1988) Hydrocarbon occurrences and structural style of the southern Suez rift basin. In: Egypt 9th petroleum exploration and production conference, EGPC, Cairo, Egypt, vol 1, pp 86–109

Knight R (1983) The use of complex plane plots in studying the electrical response of rocks. J Geomag Geoelectr 35:767–776

Knight RJ, Endres AL (1990) A new concept in modeling the dielectric response of sandstones: defining a wetted rock and bulk water system. Geophysics 55:586–594

Leila M, Moscariello A (2018) Depositional and petrophysical controls on the volumes of hydrocarbons trapped in the Messinian reservoirs, onshore Nile Delta. Egypt Petrol 4:250–267

Levitskaya MT, Sternberg KB (1996a) a, Polarization processes in rocks 1 Complex Dielectric Permittivity Method. Radio Sci 31(4):755–779

Levitskaya MT, Sternberg KB (1996b) b, Polarization processes in rocks 2. Complex Dielectric Permittivity Method. Radio Sci 31(4):781–802

Levitskaya TM, Sternberg BK (2000) Application of lumped-circuit method to studying soils at frequencies from 1 kHz to 1 GHz. Radio Sci 35(2):371–383

Moustafa AR (1996) Internal structure and deformation of an accommodation zone in the northern part of the Suez rift. J Struct Geol 18:93–107

Olhoeft GR (1985) Low frequency electrical properties. Geophysics 50:2492–2503

Orszag-Sperber F, Plaziat JC, Purser BH (1993) Factors determining Miocene evaporitic sedimentation along the Egyptian coast during Red Sea rifting. Geol Soc Egypt Spec Publ 1:143–154

Patton TL, Moustafa AR, Nelson RA, Abdine SA (1994) Tectonic evolution and structural setting of the Suez rift. In: Landon SM (ed) Interior rift basins: AAPG Memoir vol 59, pp 9–55

Radwan AE, Kassem AA, Kassem A (2020) Radwany Formation: a new formation name for the early-middle eocene carbonate sediments of the offshore October oil field, Gulf of Suez: contribution to the Eocene sediments in Egypt. Mar Pet Geol 116:104–304

Ruffet C, Guéguen Y, Darot M (1991a) Rock conductivity and fractal nature of porosity. Terra Nova 137:265–275

Ruffet C, Guéguen Y, Darot M (1991b) Complex measurements and fractal nature of porosity. Geophysics 137:758–768

Saber SG (2012) Depositional framework and sequence stratigraphy of the Cenomanian-Turonian rocks on the western side of the Gulf of Suez. Egypt Cretaceous Res 37:300–318

Said R (1990) The geology of Egypt. E.G.P.C., CONOCO, Hurghada Inc. and Repsol Expl. S. A.

Sallam ES, Ruban DA (2020) Facies analysis and depositional environments of the Miocene syn-rift carbonate-siliciclastic rock packages in the northwest Gulf of Suez. Egypt Carbon Evapor 35(1):1–20

Sellwood BW, Netherwood RE (1984) Facies evaluation of the Gulf of Suez area sedimentary history as indicator of rift initiation and development. Mod Geol 9:43–69

Sen PN (1981) Dielectric anomaly in inhomogeneous materials with application to sedimentary rocks. Appl Phys Lett 39(8):667–668

Shaltout AA, Gomaa MM, Wahbe M (2012) Utilization of standardless analysis algorithms using WDXRF and XRD for Egyptian Iron Ores identification. X-Ray Spectrom 41:355–362

Shearman DJ, Fuller JG (1969) Anhydrite diagenesis, calcitization and organic laminites, Winnipegosis Formation, Middle Devonian. Saskatchewan Bull Can Pet Geol 17:496–525

Shehata AA, Kassem AA, Brooks HL, Zuchuat V, Radwan AE (2021) Facies analysis and sequence-stratigraphic control on reservoir architecture: example from mixed carbonate/siliciclastic sediments of Raha Formation, Gulf of Suez. Egypt Marine Petrol Geol 131:105–160

Song Y, Noh TW, Lee S, Gaines R (1986) Experimental study of the three-dimensional ac conductivity and dielectric constant of a conductor- insulator composite near the percolation threshold. Phys Rev B 33(2):904–908

Tucker ME (2001) Sedimentary petrology, 3rd edn. Blackwell Science Ltd.

Vo Thanh H, Sugai Y (2021) Integrated modelling framework for enhancement history matching in fluvial channel sandstone reservoirs. Upstream Oil Gas Technol 6:100027

Vo Thanh H, Lee KK (2022) 3D geo-cellular modeling for Oligocene reservoirs: a marginal field in offshore Vietnam. J Petrol Explor Product Technol 12(1):1–19

Warren JK (2006) Evaporites: sediments, resources and hydrocarbons. Springer, Berlin

Zaid SM (2013) Provenance, diagenesis, tectonic setting and reservoir quality of the sandstones of the Kareem Formation, Gulf of Suez. Egypt J Afr Earth Sci 85:31–52